Eur. Phys. J. Plus (2025) 140:483
https://doi.org/10.1140/epjp/s13360-025-06405-x

THE EUROPEAN PHYSICAL JOURNAL PLUS

Regular Article

Exploring a forgotten heritage: the case study of Saint Vincent Martyr's simulacrum

Joana Palmeirão[1,2,a], **Margarida Nunes**[2], **Ana Manhita**[2], **Ana Curto**[2], **Luís Piorro**[3], **Eduarda Vieira**[1], **Teresa Ferreira**[2,4,b]

[1] School of Arts, Research Center for the Science and Technology of the Arts (CITAR), Universidade Católica Portuguesa, Rua de Diogo Botelho 1327, 4169-005 Porto, Portugal
[2] HERCULES Laboratory/ IN2PAST, Associate Laboratory for Research and Innovation in Heritage, Arts, Sustainability and Territory, University of Évora, Largo Marquês de Marialva 8, Évora, Portugal
[3] Laboratório José de Figueiredo, Museus e Monumentos de Portugal, Rua das Janelas Verdes, 1249-018 Lisbon, Portugal
[4] University of Évora, Chemistry and Biochemistry Department, ECT, Rua Romão Ramalho 59, Évora, Portugal

Received: 15 November 2024 / Accepted: 6 May 2025

Abstract The simulacrum of Saint Vincent Martyr, one of four *corpi santi* at the Major Seminary of Coimbra, Portugal, features Roman-origin bones mounted in metallic frameworks and covered with intricate Baroque garments. Enshrined within the urn-altar in Saint Michael's Chapel, its remains were exhumed from the Catacomb of Priscila and brought to Portugal in 1760 by Bishop Count D. Miguel da Anunciação. This study employs a multianalytical approach to examine the simulacrum's materiality, construction, and state of conservation. Non-invasive techniques, including digital radiography and borescope inspection, assessed structural integrity and skeletal arrangement. When feasible, micro-samples were collected for laboratory analysis. Optical microscopy and scanning electron microscopy with chemical analysis were used to analyse paper, textile fibres, and metal threads, revealing evidence of both craftsmanship and deterioration patterns. Additionally, Fourier-transform infrared spectroscopy characterised adhesives, coatings, and pigments, while chromatographic techniques identified dyes in garments and wax components on the face. Results corroborated photochemical damage, textile decay, and structural alterations, with in situ radiographic analyses revealing misaligned skeletal remains. Notably, softwood pulp paper with kaolin and an emerald green pigment in the flower crown points to a 19th-century local intervention after the French invasions of 1810. Furthermore, calcium carbonate in wax and lead-based pigments with iron oxides on the simulacrum's face indicate intentional methods to enhance durability and mimic human features. This study integrates material analysis with historical context to deepen understanding of Saint Vincent's simulacrum, tracing its material transformations and informing future conservation strategies for similar artefacts.

1 Introduction

The subterranean Christian burial sites in Rome were lost to history for centuries until their rediscovery on May 31, 1578, during vineyard work near Via *Salaria Nuova* [1]. This finding came shortly after the conclusion of the Council of Trent (1545–1563), which, in its final session, reaffirmed the importance of saints' and martyrs' relics as intercessors between the living and the dead [2–4]. The discovery of a remarkable, well-preserved ancient Christian hypogeum was thus perceived as a profoundly spiritual event [5, 6]. Thousands of skeletons believed to be early Christian martyrs, dubbed *corpi santi* (holy bodies) or "catacomb saints", were exhumed and sent for public veneration in churches and oratories throughout the Western Christian world [1, 5, 7]. The Roman catacombs emerged as the largest source of sacred bones, purportedly belonging to victims of Roman imperial persecutions, exceeding those listed in official martyrologies [1, 8].

From the late 17th to the mid-nineteenth century, *corpi santi* were encased in a particular type of life-sized reliquaries known as simulacra, designed to resemble the martyrs' bodies [9]. Simulacra aimed to elevate the significance of the bones they contained, viewed as powerful intercessors before God, while also promoting and reinforcing religious practice after the Protestant Reformation. Moreover, they symbolise power and influence for those who commissioned them [3, 6, 10, 11].

Metallic structures supported these remains, and their face, upper and lower limbs were crafted from gauze, papier-mâché, and wax, among others. In the first period, simulacra were dressed in Baroque-style clothing, resembling ancient Roman legionaries or virgins and displayed alongside the signs of martyrdom [1, 3]. A wide array of fabrics, passementerie like trims, fringes, and tassels,

[a] e-mail: jcpalmeirao@gmail.com (corresponding author)
[b] e-mail: tasf@uevora.pt (corresponding author)

Published online: 04 June 2025

as well as rich embroideries and lace in silk and metal threads, enhanced their presentation. Nevertheless, the quality of the textiles and complexity of the garments declined during the nineteenth century as mass production and evolving fashion trends took hold, leading to a diminished visual impact of the simulacra. The simulacra were prominently exhibited on side or main altars within polychromed, gilded wooden shrines especially commissioned for them.

During the nineteenth century, the affective piety once inspired by these reliquaries began to wane. Many simulacra were removed from their original places of worship and fell into obscurity [1, 9]. By the late twentieth century, the simulacra were serendipitously rediscovered, reigniting interest and curiosity in *corpi santi*, though only a handful of researchers engaged with this resurgence. Numerous studies have explored the excavation, acquisition, and dissemination networks of *corpi santi* from Rome to the broader Christian world [5, 12–19]. Nevertheless, few have delved into the materials and craftsmanship behind the creation of these simulacra [20–25]. In Portugal, many of these artefacts were destroyed during pivotal historical events, such as the Lisbon earthquake of 1755, the French invasions (1807–1811), the Civil War and the subsequent extinction of religious orders (1828–1834), and the establishment of the First Republic (1910). These events led to a significant loss of in situ information and contributed to the neglect, intentional damage, and decay of these religious artefacts, underscoring the paramount importance of their preservation and appreciation.

Given the complexity of these artefacts and the ethical limitations regarding their handling, non-invasive imaging techniques, such as radiography and endoscopy, have been widely employed in recent studies to examine *corpi santi* [20–25]. Notably, Kristóf and co-authors [20] conducted the first radiological study of *corpi santi* in Central Europe, examining the skeletal remains of two saints in Hungary. Their findings offered crucial insights into skeletal assembly techniques, conservation issues, and decorative elements such as embroidery and metallic ornaments, directly informing subsequent restoration efforts. Similarly, Alterauge and co-authors [21] identified sophisticated metal frameworks and iron rods that supported the anatomical positioning of bones, highlighting the technical expertise of the artisans who assembled the relics. These findings align with earlier observations by Pfeiffer [23] and Palmeirão [25, 26], who documented similar structural reinforcements, including small wires securing bones. Pfeiffer [23] further expanded this research by conducting a comprehensive technical-material study on several simulacra in Germany, while Palmeirão [25, 26] applied similar methodologies to Portuguese examples.

This study investigates the simulacrum of Saint Vincent Martyr from the Major Seminary of Coimbra, Portugal, employing a multidisciplinary approach to assess its material composition, construction techniques, and state of conservation. Combining imaging techniques and material analysis, it explores the simulacrum's layered structure, material composition, and degradation state. Non-invasive techniques, including digital radiography and borescope inspection, were employed to evaluate its structural integrity, internal skeletal arrangement, and the presence of structural reinforcements. When possible, samples were collected for in-lab analysis, including optical microscopy (OM) and scanning electron microscopy combined with chemical analysis (SEM-EDS) to examine paper, textile fibres, and metal threads, providing insights into original craftsmanship and conservation state. Fourier-transform infrared spectroscopy (FTIR) was used to characterise adhesives, coatings, and pastes. To further investigate organic components, high-performance liquid chromatography with diode array and mass spectrometry (LC-DAD-MS) was employed for dye identification in garments and textile decorations, while pyrolysis–gas chromatography coupled with mass spectrometry (Py-GC-MS) was crucial for identifying wax elements from the face. By integrating these methodological approaches, this study has deepened the understanding of Saint Vincent's simulacrum, shedding light on its modifications and informing future conservation strategies.

2 Historical context

According to the official authentication document (*autentica*), the *sacrum corpus* (sacred body) of Saint Vincent Martyr was exhumed from the Catacomb of Priscila in 1760 and offered to D. Miguel da Anunciação, Bishop-Count of Coimbra (1741–1779) and founder of the Major Seminary (Fig. 1a). This document, issued by Cardinal-Vicar Antonio Maria Erba Odescalchi (1759–1762) and Custodian of the Sacred Relics (1751–1773), provides crucial historical context, detailing the transfer of the relics by order of Pope Clement XIII (1758–1769) and outlining the conditions under which they were bestowed.

The *autentica* also revealed that the holy body of Saint Vincent was carefully placed "in a white wooden box, well-sealed and tied with a red silk cord" before being formally handed over to the "Illustrious and Reverend Bishop of Coimbra". This highlights the care and reverence with which the relics were handled upon their exhumation from the catacombs. However, it notably omits details about the simulacrum encasing the relics. Typically, such relics were housed in simulacra after their authentication—a process overseen by Church authorities to ensure proper respect and preparation [26]. The simulacra were meticulously crafted to represent the martyr physically. The lack of information in the Seminary's archive regarding whether the simulacrum was assembled in Rome—where many catacombs' relics were traditionally prepared for exhibition—or if it was a national creation leaves this aspect of the Saint Vincent relics shrouded in mystery.

During the French Invasions, particularly the Second Invasion in 1810, the Seminary of Coimbra faced severe disruptions. Under Marshal André Masséna's command, French troops occupied the city, repurposing the Seminary's buildings for military use. This occupation caused significant material and cultural losses. The troops looted the Seminary, desecrating and destroying many sacred relics kept in reliquaries [27].

Fig. 1 **a** Authentication document of Saint Vincent Martyr's relics, Major Seminary of Coimbra Archive; **b** simulacrum of Saint Vincent Martyr in the main altar of the Saint Michael's Chapel, Major Seminary of Coimbra, Portugal

Recent archival documentation uncovered during restoration works in 2024 has further confirmed the extent of the damage inflicted by French troops. These documents provide a detailed account of the desecration of relics, revealing that the French soldiers removed the remains of Holy Martyrs Fortunatus and Liberatus from their coffins, damaged them, and tore apart their garments. The same fate befell the relics of Saint Vincent in Saint Michael's Chapel, along with many others stored in reliquaries throughout the chapel [28]. This devastation symbolises the broader cultural and spiritual destruction wrought by the French occupation, highlighting the profound impact of the invasions on the Seminary and its heritage.

3 Materials and methods

3.1 Location and description of the simulacrum

The simulacrum of Saint Vincent Martyr is displayed on the altar of the Saint Michael's Chapel, located on the second floor of the Major Seminary of Coimbra. Positioned horizontally and supine, the body faces left, with the head slightly tilted to the right and resting on a dark blue velvet cushion trimmed with gold that enhances its solemnity (Fig. 1b). Measuring approximately 125 cm in length and 60 cm in width, the simulacrum is housed within a glass-fronted Rococo-style wooden altar, which is richly polychromed and gilt. This design facilitates detailed observation while maintaining a sense of sacredness.

The simulacrum features a polychromed wax mask with an orange-brown hue, displaying facial features including a flattened chin, prominent closed lips, a pronounced nose, and deep-set closed eyes. A crown of coloured paper flowers intertwined with silver-gilt threads adorns the head. The body is dressed in a patterned taffeta tunic embroidered with floral motifs interwoven with golden and silver threads, cinched at the waist by a blue satin belt. A salmon-tone satin mantle with geometric and floral patterns covers the shoulders and extends to the feet, edged with lace trim for a cohesive appearance.

The hands and feet are adorned with silver metal lace gloves and socks, with the hands positioned over the abdomen. The legs extend straight, with the feet aligned vertically and fitted with open sandals featuring crisscrossed straps. A blue fabric drapes the platform beneath the simulacrum, while the trapezoidal support beneath the cushion is wrapped in the same fabric as the tunic, creating a seamless and harmonious visual composition.

A Latin inscription, "S S.mus CHRISTI MARTYR VINCENTIVS", is painted on a fabric cartouche measuring approximately 32 cm in width by 25 cm in height, affixed to the back wall of the altar, highlighting the simulacrum's identity and religious significance.

3.2 Sampling

A total of 28 samples were collected to characterise the materials used in the upper limbs, garments, and accessories of Saint Vincent's simulacrum (Table 1 and Fig. SI.1). These samples were categorised into key groups: wax (face mask), textile fibres and metal threads (garments, cushion, and cartouche), and paper (flower crown). Each sample was carefully selected to represent a specific material or element of the simulacrum's construction, ensuring a comprehensive understanding of its diverse components. Sampling was limited to areas with pre-existing damage or loose elements to preserve the integrity of the artefact. Laboratory analyses were subsequently performed to investigate the morphology, chemical composition, structural properties, and potential degradation mechanisms.

Table 1 Sample identification (ID), item classification (e.g. face mask, garments, accessories), description of samples collected from Saint Vincent's simulacrum, and analytical techniques employed

ID	Item	Type	Description	Colour	Analytical techniques*
Vt1	Face mask	Wax	Neck	Orange–brown	OM, ATR-FT-IR, Py-GC-MS, SEM-EDS
Vt2	Face mask	Wax	Hair	Dark brown	OM, ATR-FT-IR, SEM-EDS
Vt3	Flower crown	Paper	Leaf	Green	OM, LC-DAD-MS, ATR-FT-IR
Vt4	Tunic	Textile fibre	Silk fibre|weft and warp fibres (degraded area)	Beige	OM, SEM-EDS
Vt5	Tunic	Textile fibre	Silk fibre|weft and warp fibres	Beige	OM
Vt6	Body	Textile fibre	Vegetable filling, hemp	Light ochre	OM
Vt7	Tunic	Metal thread	Floral motifs|strip wound around a silk core	Silver strip Green core	OM, LC-DAD-MS, SEM-EDS
Vt8	Tunic	Textile fibre	Floral motifs|silk fibre	Yellowish salmon	OM, LC-DAD-MS
Vt11	Neck (inside)	Fabric	Silk fibre|fibre with wax clusters attached	Orange–brown	OM
Vt12	Tunic	Textile fibre	Floral motifs|silk fibre	Dark pink	OM
Vt14	Mantle	Metal thread	Lace trim|strip wound around a silk core	Gilt strip Yellow core	OM, SEM-EDS
Vt15	Tunic	Textile fibre	Floral motifs|silk fibre	Dark brown	OM, LC-DAD-MS, SEM-EDS
Vt16	Tunic (sleeve)	Metal thread	Lace trim|strip	Silver strip	SEM-EDS
Vt17	Tunic (sleeve)	Metal thread	Lace trim|strip wound around a silk core	Silver strip Yellow core	OM, SEM-EDS
Vt18	Mantle	Textile fibre	Lining fabric|silk fibre	Salmon pink	OM, LC-DAD-MS
Vt19	Cushion	Textile fibre	Silk fibre	Dark blue	OM, LC-DAD-MS
Vt22	Platform	Textile fibre	Silk fibre|weft and warp fibres	Blue	OM, LC-DAD-MS
Vt23	Mantle	Textile fibre	Floral motifs|silk fibre	Light green	OM, LC-DAD-MS
Vt24	Glove	Metal thread	Metal lace|strip wound around a silk core	Gilt strip White core	OM, SEM-EDS
Vt25	Sock	Metal thread	Metal lace|crimp thread	Gilt strip Yellow core	OM, SEM-EDS
Vt26	Left femur	Paper	Cardboard tube	Light brown	OM, ATR-FT-IR
Vt28	Mantle	Textile fibre	Floral motifs|silk fibre	Green	OM, LC-DAD-MS
Vt29	Mantle	Textile fibre	Floral motifs|silk fibre	Yellow	OM, LC-DAD-MS
Vt30	Mantle	Metal thread	Floral motifs|strip wound around a silk core	Silver strip Blue core	OM, LC-DAD-MS, SEM-EDS
Vt32	Fabric cartouche	Textile fibre	Silk fibre	Light salmon pink	OM
Vt33	Fabric cartouche	Ink	Inked cartouche	Light salmon pink	OM, ATR-FT-IR, SEM-EDS
Vt35	Platform	Textile fibre	Fabric bow, silk fibre	Salmon pink	OM, LC-DAD-MS
Vt36	Belt	Textile fibre	Silk fibre	Blue	OM, LC-DAD-MS

*The acronyms for the names of analytical techniques are explained in the following subsections

3.3 Digital photography and in situ radiography

A full-body picture was obtained with a Mamiya RZ67 Pro II camera with a Mamiya-Sekor 65 mm f:4 lens and a Sinar 44 sensor under 2×1000 W tungsten lights. Detailed images of the simulacrum were also obtained with a Nikon D3000 digital camera.

A portable X-ray generator (Yxlon Andrex Smart 160) and a Scanna CR35 digitalisation system were used for the in-situ digital radiographic examination. The X-ray source was positioned at 310 cm from the flexible X-ray plates affixed to the altar behind the simulacrum. In addition to full-body scans, partial head, pelvis, and feet exposures were performed. Exposures were obtained with a current intensity of 5 mA at peak voltages of 30 kV and 40 kV for 5 and 10 min, respectively. The penetrating power of X-rays enabled a non-invasive, non-destructive examination of the artefact's internal structure, recording the different material densities.

3.4 In situ visual inspection and optical microscopy (OM) analysis

The visual inspection of the simulacrum provided an initial assessment of the materials' nature and conservation state, as well as a preliminary understanding of production and assembly techniques. In situ digital microscopy analysis was conducted using a digital handheld AM7515MZT Dino-Lite Edge (©AnMo Electronics Corporation, Taiwan) with a 20× to 200× magnification

range. Visual inspection of the simulacrum internal structure was done with a portable inspection camera or borescope (©ChiliTec GmbH, Lehre, German) with 1080P resolution, a semi-rigid 5 m USB cable, Ø8 mm lens, and six adjustable LED lights.

High-resolution digital microscopy of the samples was performed at the laboratory using a 3D Hirox RH-2000 digital microscope (©Hirox Europe, France) with an MXB-5040RZRZ revolver zoom lens. The image acquisition occurred at magnifications ranging from 140× to 400×, with top-light illumination and Hirox™ software.

Fibre analysis was conducted with a Leica DM2500M dark-field microscope (©Leica Microsystems GmbH, German) coupled to a Leica MC170 HD digital camera and a Meiji MT bright-field (©Meiji Techno, Japan) microscope paired to a Dino-Eye eyepiece camera (©AnMo Electronics Corporation, Taiwan). Both 100× and 200× magnifications were used. For further identification, the twist test was performed on plant fibres following the methodology of Wiener, Kovacic, & Dejlová [29].

3.5 Attenuated total reflection Fourier-transform infrared spectroscopy (ATR-FT-IR)

ATR-FT-IR analysis was done on samples collected from the face mask (wax) and the flower crown (paper) to identify inorganic and organic compounds. Infrared analyses were performed on a Bruker Alpha spectrometer (Bruker™ Optics and Microanalysis GmbH, Germany) controlled by OPUS 6.5 software and coupled with a single-reflection diamond ATR module. An ATR mode was used in the 4000–350 cm^{-1} region, with 4 cm^{-1} spectral resolution and 128 scans. Published data and the IRUG database were used for spectra interpretation.

3.6 Natural dyes' extraction procedure

Dyed samples (approximately 2.0 mg) were placed in vials, and 1.0 mL of a 0.1% EDTA solution in water/DMF (1:1, v/v) was added. The vials were sealed and kept at 100 °C for 30 min. The solvent was then removed by freeze-drying. Dried samples (except for blue/green colours) were re-dissolved in 250 μL of MeOH/H_2O (1:1, v/v). Blue/green samples were re-dissolved in 250 μL of MeOH/DMF (1:1, v/v). After re-dissolution, all samples were filtered through a 0.45 μm PTFE filter prior to HPLC analysis.

3.7 High-performance liquid chromatography coupled with a diode array and mass spectrometry detection (LC-DAD-MS)

The dye sources used for dyeing the fibres in the garments and accessories (cushion, platform and flower crown) were evaluated using the LC-DAD-MS technique. A Thermo Finnigan LCQ Fleet mass spectrometer instrument equipped with an ESI source, an ion trap mass analyser, and a PDA detector was used for the analyses. The MS analysis conditions were as follows: capillary temperature of 300 °C, source voltage of 5.0 kV, source current of 100.0 μA, and capillary voltage of −3.0 V in negative ion mode and 22.0 V in positive ion mode. Analytes were detected in full MS mode (m/z 100–800), with fragmentation at the ion source. For the negative ion mode, two source-induced dissociation (SID) segments were utilised: 10.0 V SID from 0 to 12 min and 30.0 V CID from 12 to 30 min; for the positive ion mode, 30.0 V SID was used from 0 to 30 min. The column and the tray temperatures were set at 30 °C and 24 °C, respectively. The DAD detector operated in the range of 200–800 nm. The MS and DAD instruments were coupled to an LC system with a Surveyor Thermo Finnigan autosampler. The analytical column was a reversed-phase Agilent Zorbax Eclipse XDB-C18 (C18, 3.5 μm particle size, 150 × 2.1 mm). The mobile phase consisted of acetonitrile (A) and water acidified with 0.1% formic acid (B). The gradient elution was 0–63% A from 0–14 min, then 63–90% A from 14 to 25 min and 90% A from 25 to 30 min. A 0.2 mL/min mobile phase flow was used, and the injection volume was set to 20 μL.

3.8 Pyrolysis-gas chromatography coupled with mass spectrometry (Py-GC-MS)

A wax sample from the face mask was analysed using the Py-GC-MS technique. A system with a Frontier Lab PY-3030D double-shot pyrolyser was used, with the interface set at 280 °C. The pyrolyser was coupled to a Shimadzu GC2010 gas chromatographer and connected to a Shimadzu GCMS-QP2010 Plus mass spectrometer. A Phenomenex Zebron ZB-5HT capillary column (30 m length, 0.25 mm internal diameter, 0.50 μm film thickness) was used for separation, with helium as the carrier gas, adjusted to a flow rate of 1.5 mL/min. The split injector (15:1 ratio) operated at 250 °C. The GC temperature programme was as follows: 35 °C for 1 min, followed by a series of temperature ramps: until 110 °C at 60 °C/min, until 240 °C at 14 °C/min, up to 280 °C at 6 °C/min, and finally until 320 °C at 30 °C/min, and then an isothermal period of 6 min. The ion source temperature was placed at 240 °C, and the interface temperature was maintained at 280 °C. The mass spectrometer was programmed to acquire data between 40 and 1090 m/z. Sample (< 200 μg) was previously derivatised with 3 μL of tetramethylammonium hydroxide (TMAH, 2.5% in MeOH) in a 50-μL Eco-cup capsule. The capsule was then placed in the pyrolysis and pyrolysed at 500 °C. Compound identification was performed using AMDIS software, integrated with the NIST20 and Wiley7 spectral libraries.

3.9 Scanning electron microscope coupled with energy-dispersive X-ray spectroscopy (SEM-EDS)

For morphologic and chemical characterisation of the metal threads, textile fibres, and paper (flower crown), analyses were carried out on a variable pressure Hitachi™ S-3700N SEM (Hitachi High-Tech® Europe GmbH, Germany) coupled with a Bruker™ XFlash 5010 SDD EDS® spectrometer (Massachusetts). The resolution of the EDS detector is 123 eV at the Mn Kα energy line.

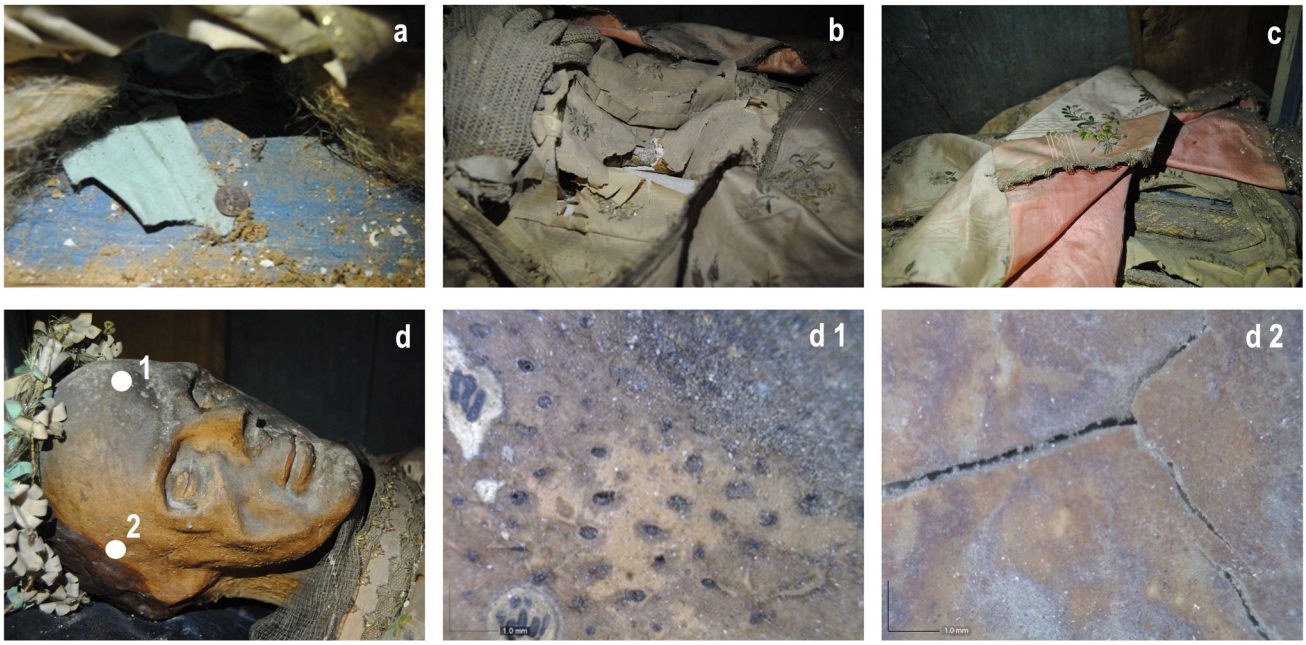

Fig. 2 Detailed photographs of the **a** extensive dirt accumulation, **b** deterioration of the tunic fabric, and **c** pronounced discolouration of the mantle. Digital in situ microscopic images of the face's polychromed surface damages, including whitish spots, **d1** pitting, and **d2** cracks

The metal threads were analysed under a pressure of 40 Pa. An accelerating voltage of 20 kV was used for the chemical analyses and imaging in the backscattered mode (BSE). For the textile fibres analysis, the samples were coated with carbon and the analyses were conducted under a high vacuum. Acceleration voltages of 10 kV and 20 kV were used for imaging in secondary electron mode (SE) and point analysis for the mordant identification, respectively. Semiquantitative data on elemental composition were obtained using Esprit1.9® software. Three EDS point analyses for the textile fibres and EDS area analyses for metal threads and paper were performed to ensure data representativeness.

4 Results

4.1 Visual inspection

A preliminary assessment of the simulacrum revealed several conservation issues, primarily due to the extensive accumulation of dust, dirt, lint, sawdust, dead insects, paper fragments, and other debris. Furthermore, rusty metal tacks were identified (Fig. 2a). The visual inspection also revealed apparent significant alterations to the simulacrum. The positioning of both legs suggests that it was adjusted to fit snugly within its glass-fronted wooden urn, indicating that it was not originally intended for this altar but was relocated here at some point. Furthermore, the differing assembly materials used for each femur suggest a prior reconstruction effort had occurred. Historical records note that during the French invasions in 1810, the relics of Saint Vincent were trampled, also leading to the displacement and fractures observed in the leg bones. This context helps explain the necessity for such an intervention.

4.1.1 Textile materials

The textiles show pronounced deterioration, exhibiting significant pathologies such as deep lacerations, discolouration, and loss of cohesion of the tunic fabric (Fig. 2b). The severe discolouration and cohesion loss are presumed to result from prolonged exposure to intense light and photochemical degradation from UV radiation. Likely, the simulacrum was previously displayed in a brightly lit environment, a hypothesis also supported by the substantial accumulation of dirt and wax drips on the tunic's surface, inconsistent with its current display conditions. The damage from the French invasions also likely contributed to accelerating the tunic's decay. Furthermore, the mantle that overlaps the tunic shows notable discolouration (Fig. 2c), along with localised moisture stains and wax drippings.

Fig. 3 Digital photographs of Saint Vincent's simulacrum indicating **a** and **a*** the area of inclination of the leg bones, and detailed photographs of the assembly system of the **b** femurs and **c** the right foot

4.1.2 Polychromed wax surface

The polychromed surface of the face has experienced extensive oxidation and darkening due to prolonged exposure to dirt and material degradation (Fig. 2d). Additionally, the presence of whitish spots, pitting, cracks, and fissures further detracts from the overall appearance of the face (Fig. 2d1, d2).

4.1.3 Osteological analysis

Inspection of the bones visible through the damaged tunic fabric revealed significant structural issues. Notably, the bones of both legs, specifically the tibia and fibula, exhibit a marked inclination, suggesting they were deliberately repositioned to fit within the altar (Fig. 3a*), as previously mentioned. Indeed, the simulacrum fits snugly, with the feet resting vertically against the altar's sidewall, and the overall length of the body is noticeably shorter than other recumbent examples (Fig. 3a and c). The access challenges from the rear of the altar suggest that the simulacrum was likely inserted through the front opening of the urn-altar, requiring adjustments to the bones to accommodate its current position.

Additionally, a *post-mortem* fracture in the right femur was detected, appearing misplaced and inverted, with the fracture exposing the trabecular bone (Fig. 3b). The right foot bones reveal a high degree of disorganisation and fragmentation, likely resulting from impact or displacement, potentially related to the traumatic event that caused the femoral fracture (Fig. 3c). Furthermore, a *post-mortem* fracture was observed in the right wrist, involving the radius or ulna, suggesting that the upper or lower limbs on the right side (forearm, thigh, leg, and foot) were subjected to significant impact, leading not only to the repositioning of the limbs but also to the fractures in most of the observable bones.

In a similar observation, the hand bones appear to be fused with a dark adhesive paste. It is unclear whether these bones are metacarpals or metatarsals; however, they are misaligned, with the proximal extremity positioned distally. Macroscopic examination also reveals that the tarsal bones are attached with a waxy brownish-grey material.

4.1.4 Assembly technique

Detailed observations revealed that the left femur is wrapped in a cardboard tube secured with sisal thread, providing structural reinforcement, a feature absent in the right femur. In contrast, the right femur shows a waxy, greyish-brown paste at its upper end (Fig. 3b), a substance also found in the foot bones. It remains unclear whether this waxy material was initially applied to stabilise or protect the bones or if it was part of a later effort to consolidate them after major damage.

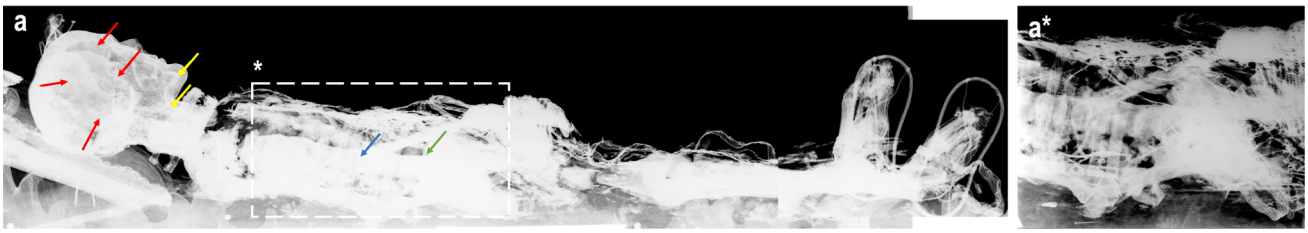

Fig. 4 **a** General radiography of Saint Vincent's simulacrum marked with coloured arrows; and **a*** detailed radiography of the chest

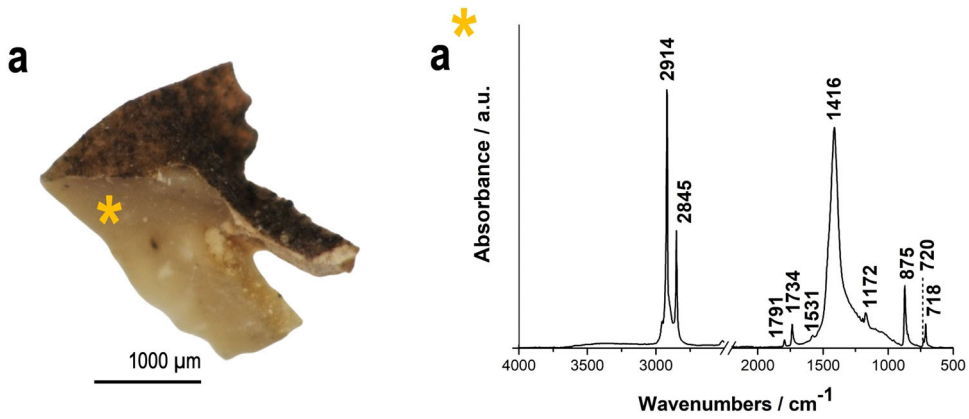

Fig. 5 **a** High-resolution digital microscopic image of the wax sample Vt1 from Saint Vincent's neck; **a*** corresponding FT-IR spectrum, revealing the characteristic features of beeswax and calcium carbonate

4.2 In situ radiography

The cranium appears fragmented in the digital radiography (Fig. 4, red arrows), with a notable absence of both facial bones and dentition. However, a distinct structure delineating the chin and neck contours remains visible (highlighted by yellow arrows).

In the thoracoabdominal region, several dorsal vertebrae (blue arrow) and ribs appear to be glued or pasted together, as their margins are poorly defined, possibly similar to that observed in the hand bones (Fig. 4a, a*). The right humerus and radius (arm and forearm) are also identifiable, along with what appears to be part of the left radius. The *os coxae* (green arrow) also seems to be present. Thick wires are visible at the elbow, likely serving to stabilise the bone fragments, and similar components are found in the hip region. Apart from these metallic elements, no internal metallic structures were identified, which is atypical of the construction methods commonly seen in Roman-origin simulacra.

In the lower limbs, the distal end of the displaced right femur was identified, alongside the right fibula and tibia, as well as the femur and fibula of the left leg. The foot bones are incomplete, consisting of only some metatarsals and phalanges. While certain bones, such as the metatarsals and phalanges of the first digit, are correctly positioned, other phalanges are visibly out of place (Fig. 3c).

4.3 Materials characterisation

4.3.1 Wax

SEM-EDS and ATR-FT-IR techniques were used to investigate the materials composing the face mask, with the neck included. Beeswax has been one of the oldest and most widely used natural waxes, particularly in manufacturing materials for artistic and symbolic purposes [30–32]. Its hydrophobicity and plasticity made it ideal for modelling the face and upper and lower limbs. However, little is known about its application in the manufacture of simulacra, and its analytical characterisation remains surprisingly scarce [26, 33, 34].

Characteristic bands indicative of a wax-based material were identified in sample Vt1 (Fig. 5). The FT-IR spectrum was dominated by features associated with hydrocarbons and fatty acids. Specifically, the hydrocarbon bands were observed at *ca.* 2914 cm^{-1} ($\nu_{as}CH_2$), 2845 cm^{-1} ($\nu_{s}CH_2$), with a smooth shoulder at *ca.* 1463 cm^{-1} (scissoring CH_2), and a doublet at 720 cm^{-1} and 718 cm^{-1} (rocking CH_2). Additionally, bands corresponding to νC=O and νC–O attributed to fatty acids and esters were identified at *ca.* 1734 cm^{-1} and 1172 cm^{-1}, respectively. This vibrational pattern supports the attribution to beeswax [35, 36].

Py-GC-MS analysis was conducted on sample Vt1 to further explore the wax mask composition. The pyrogram (Fig. SI.2) shows a distribution of some classes of compounds that are compatible with beeswax: odd-numbered n-alkanes (C21–C33) peaking at C27; even-numbered fatty acids (C22–C34) with lignoceric acid C24 being the main fatty acid; even-numbered wax esters in the

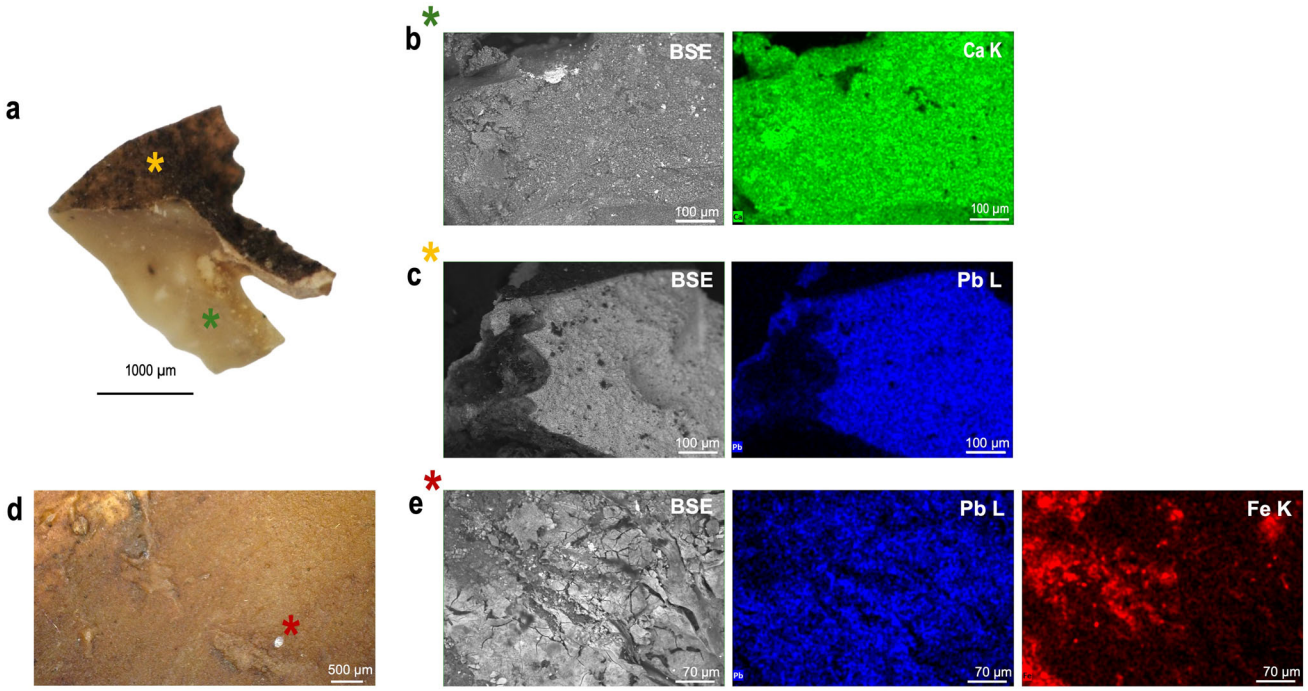

Fig. 6 **a** High-resolution digital microscopic image of Vt1 sample, **b*** BSE micrograph and Ca elemental mapping illustrate that the inner layer of the wax is enriched in calcium, and **c*** EDS elemental mapping highlights the distribution of Pb in the outer layer of the wax; **d** digital microscopic image of polychromed wax from the painted hair (Vt2), and **e*** BSE micrograph of the brownish area, with the Fe and Pb elemental mapping

range C40–C52 (Fig. SI.3) [37]. The pyrogram of sample Vt1 is provided in the Supplementary Information section (Fig. SI.2), and the mass spectrum of the wax ester C40 is included in Fig. SI.3 to confirm its presence following pyrolysis at 500 °C.

Traditionally, various additives have been mixed with wax-based artefacts [38, 39]. Starch or flour was employed to reduce the amount of expensive beeswax, while paraffin and resins were commonly added as hardeners [38, 40]. Aesthetic properties were often enhanced by introducing pigments [38, 39]. No resin, protein or carbohydrate biomarkers were detected, which led us to conclude that no organic additives seemed to have been added to the wax. Paraffin is described as a series of odd and even-numbered n-alkanes, C21–C35, peaking at C27. The greatest challenge in identifying paraffin wax arises when it is mixed with other waxes, which mask its presence and, therefore, the (remote) possibility of mixing paraffin with beeswax cannot be excluded. An inorganic compound, calcium carbonate, was identified through FT-IR and SEM-EDS analysis. Characteristic bands of $CaCO_3$ were observed at *ca.* 1416 cm^{-1} ($\nu_{as}CO_3$, ν_4 mode), 875 cm^{-1} ($\nu_{as}CO_3$, ν_2 mode), and 720 cm^{-1} (ν_sCO_3, ν_4 mode) [41], indicating this compound was incorporated as an extender in the wax-making process. Moreover, EDS mapping analysis showed a uniform distribution of Ca across the innermost layer of the sample, confirming the deliberate addition of this extender to the wax material (Fig. 6). Calcium carbonate enhances the physical properties of the wax, improving its malleability and workability [42]. Once shaped and dried, the extender contributes to the material's rigidity, helping it retain its form. However, some degradation effects, such as shrinkage and embrittlement, may occur [40]. Additionally, calcium carbonate contributes to the opacity of the wax [38].

Furthermore, Saint Vincent's face mask, with the neck included, exhibited a polychromed surface with yellowish and brownish hues mimicking skin (Vt1) and hair (Vt2), respectively (Fig. 2d). EDS analysis identified a Pb-enriched layer evenly distributed over the outermost areas of the face and neck, suggesting the use of a lead pigment to achieve a whitish hue (Fig. 6c*). Unfortunately, the sample was fragmented, and the small size of the pieces, combined with the wax matrix, compromised the quality of the Raman analysis, which is essential for accurately determining the pigment's nature. Nonetheless, a particular lead pigment, white lead, is documented [38, 43] as commonly used in wax-artistic sculptures and anatomical models from the 16th to the nineteenth centuries, often employed in various colours to achieve different hues [40]. The presence of Pb in our samples also accounts for the pronounced opacity observed in the X-ray images (Fig. 4a). The darkening effect may be associated with the formation of lead sulphides, which typically present as black or brown due to reactions between Pb and sulphur oxides in the surrounding environment [44]. Moreover, the presence of lead and calcium soaps may further contribute to this effect [45]. In the FT-IR spectrum (Fig. 5a*), a smooth shoulder at *ca.* 1531 cm^{-1} ($\nu_{as}COO^-$) suggests the presence of carboxylates, likely resulting from the formation of soaps, such as calcium or lead palmitate and stearate. The saponification of wax esters in beeswax, or the influence of certain environmental factors, may promote soap formation—similar to the degradation observed in oil paintings due to pigment-induced saponification [46]. However, distinguishing between these compounds was challenging due to peak overlapping. Furthermore, palmitone was also identified in this sample through Py-GC-MS analysis.

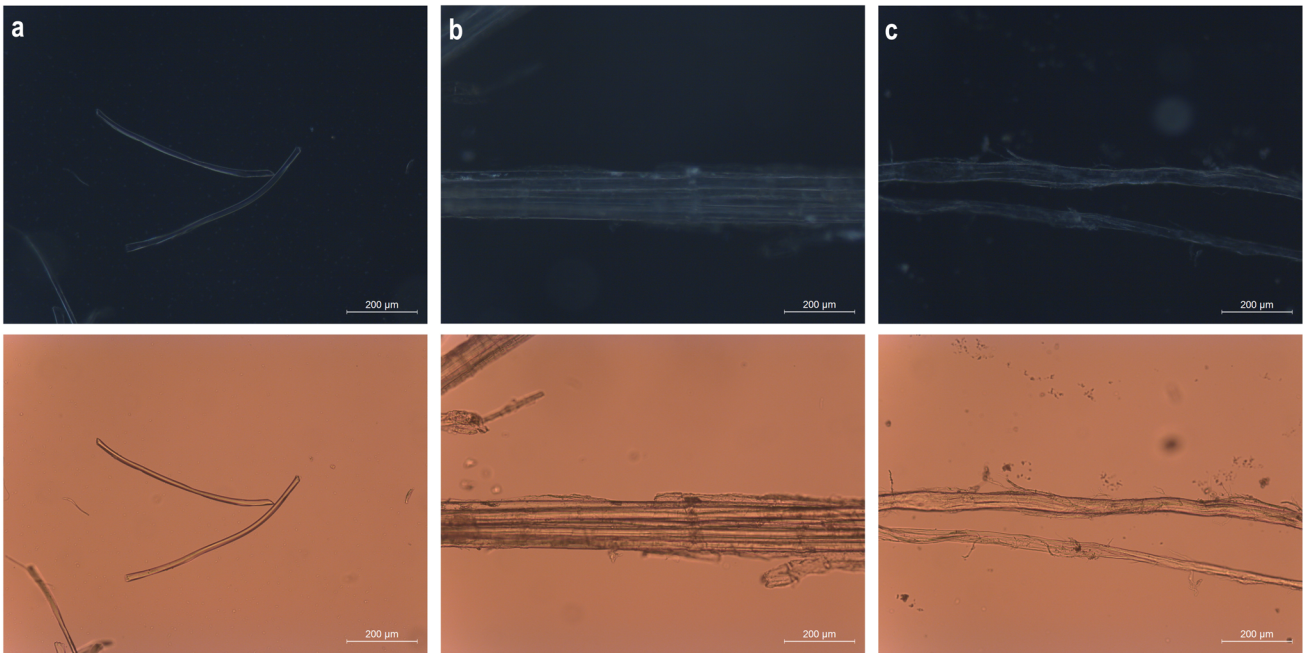

Fig. 7 Dark-field (top) and bright-field (bottom) analysis of fibre samples **a** Vt17, **b** Vt6, and **c** Vt26, respectively

Iron was also detected in the coloured areas intended to mimic hair, indicating the presence of a Fe oxide-based pigment as a red ochre (Fig. 6e*). The use of red iron pigments as colourants for wax is also documented in the literature [40]. However, to the author's knowledge, there is a lack of specific information regarding the application of these pigments wax bodies of simulacra.

4.3.2 Textile fibres

Dyes analysis The LC-DAD-MS analysis of thirteen samples (Table 2) from the garments and accessories of the simulacrum highlights the predominant use of weld (*Reseda luteola* L.) for yellow and green colours (Vt7, Vt28 and Vt29), often combined with indigo or woad to produce green hues. Yellow sample Vt29 contained several luteolin derivatives and apigenin, a profile characteristic of weld. This is consistent with the historical use of *Reseda luteola* L. for producing vibrant yellow colours [47]. In yellow sample Vt8, only isorhamnetin-3-O-glucoside was tentatively identified, which is not typical of weld and suggests an alternative flavonoid-based dye source. For the blue colour (Vt22, Vt30 and Vt36), indigo or woad was identified as the primary dye. The brown sample Vt15 showed the presence of a quercetin-glucoside along with luteolin and apigenin glucosides. A quercetin derivative suggests a flavonoid-based dye diverse from weld, which may indicate using a different plant dye or a mixed dyeing process. Quercetin- and luteolin-based dyes are known to yield yellow shades that can appear brownish when iron mordants are applied [47]. This is supported by the detection of an iron mordant in the Vt15 sample through SEM-EDS analysis (Fig. SI.4).

In four coloured samples (Vt18, Vt19, Vt23 and Vt35), no chromophores were detected, suggesting that the extraction procedure may have been ineffective in retrieving the dyes and their degradation products, if present, leading to concentrations below the instrument's detection limits. Similarly, no chromophore was observed in Vt3, a leaf from the crown sample. However, as discussed in subchapter 4.3.5, this sample was painted with an inorganic pigment that is not detectable by LC-DAD-MS analysis.

Fibre analysis The examined fibres included silk fibres used for decoration and fibrous cores of the metal threads, which were also made of silk (Table 1). Both the fibrous filling utilised to add volume to the simulacrum body (Vt6) and the paper sample from the cardboard tube that encased the left femur and shaped the leg (Vt26) were identified as plant fibres. Notably, the twist test confirmed that sample Vt6 is a hemp aggregate. Figure 7 presents representative dark-field and bright-field microscopic images of analysed fibres (Vt17, Vt6 and Vt26).

SEM inspection was conducted on a sample from a degraded area of the tunic fabric (Vt4) consisting of weft and warp fibres. The fibre fractures were described following Hearle's classification system [48], with related literature [49, 50] utilised for comparison and further discussion. The sampling procedure guaranteed the original integrity of the sample.

The silk fibres are nearly cylindrical, with diameters ranging from 10 to 20 µm, consistent with the reported literature [48, 51]. Figure 8 illustrates the morphological features of the silk fibres where the predominant fracture types are shown. In the weft fibres, fatigue-related damage was observed, illustrated by a flex-fatigue split (Fig. 8a). Over time, fibres subjected to folding become more prone to flex fatigue, leading to breakage under slight pressure. This phenomenon was particularly evident in the folded sections of

Table 2 LC-DAD-MS identification of natural dyes in samples collected from the garments and accessories of the simulacrum of Saint Vincent Martyr

Location	Sample ID/colour	Retention time (min.)	λ máx (nm)	$[M-H]^-$ (m/z)	Peak identification	Possible dye source
Crown	Vt3/green	–	–	–	–	No chromophore detected
Tunic	Vt7/green	16.04	335	609, 447, 285	Luteolin-di-O-glucoside	Weld + Indigo or Woad
		16.75	345	447, 285	Luteolin-7-O-glucoside	
		19.41	347	285, 151, 133	Luteolin	
		20.50	332	269, 151, 117	Apigenin	
		23.95	607	263, 219 (positive mode)	Indigotin	
	Vt8/yellowish salmon	15.77	380	477, 459	Isorhamnetin-3-O-glucoside (?)	Flavonoid dye source
	Vt15/dark brown	16.58	370	463, 301	Quercetin-glucoside	Flavonoid dye source
		16.75	345	447, 285	Luteolin-7-O-glucoside	
		17.66	340	447, 431, 285, 269	Luteolin-O-glucoside + Apigenin-O-glucoside	
Platform	Vt35/salmon pink	–	–	–	–	No chromophore detected
Mantle	Vt22/blue	23.95	607	263, 219 (positive mode)	Indigotin	Indigo or Woad
	Vt30/blue					
	Vt23/light green	–	–	–	–	No chromophore detected
	Vt28/green	16.04	335	609, 447, 285	Luteolin-di-O-glucoside	Weld + Indigo or Woad
		16.75	345	447, 285	Luteolin-7-O-glucoside	
		19.41	347	285, 151, 133	Luteolin	
		20.50	332	269, 151, 117	Apigenin	
		23.95	607	263, 219 (positive mode)	Indigotin	
	Vt29/yellow	16.04	335	609, 447, 285	Luteolin-di-O-glucoside	Weld
		16.75	345	447, 285	Luteolin-7-O-glucoside	
		19.41	347	285, 151, 133	Luteolin	
		20.50	332	269, 151, 117	Apigenin	
Mantle (lining)	Vt18/salmon pink	–	–	–	–	No chromophore detected
Belt	Vt36/blue	23.95	607	263, 219 (positive mode)	Indigotin	Indigo or Woad
Cushion	Vt19/dark blue	–	–	–	–	No chromophore detected

the tunic fabric, where combination-type fractures prevailed. These included fractures in highly oriented fibres (Fig. 8b) and those caused by multiple splits along the fibre (Fig. 8c). Interestingly, surface peeling, a common degradation issue in historic silk textiles, was not observed in this case [48].

Various fracture types were observed in the warp fibres, including ductile and surface-flaw-influenced fractures, as depicted in Fig. 8d and e, respectively. The predominant fracture mechanisms were governed by surface flaws, while brittle and granular fractures, as well as void formations, were observed to a lesser extent (Fig. 8f). According to Bresee & Goodyear [49], radiation exposure is critical in silk fibre degradation, particularly in the formation of surface flaws. These findings suggest that the deterioration of Saint Vincent's silk fabrics was primarily influenced by prolonged exposure to inappropriate radiation, as though during visual inspection. Notably, the predominant degradation mechanism in naturally aged silk fibres appears to be the loss of interfibrillar

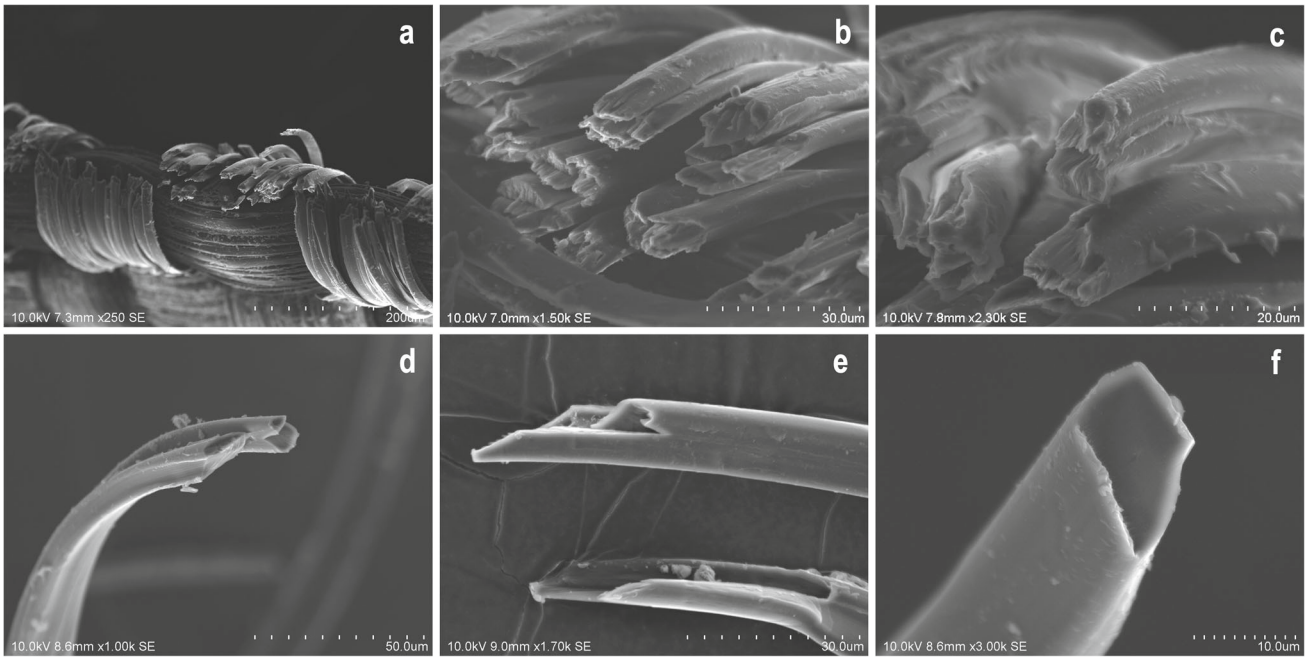

Fig. 8 SEM micrographs of various silk fibre fractures from sample Vt4: **a**–**c** fractures in the weft fibres caused by flex and twist fatigue, and **d**–**f** fractures in the warp fibres, including ductile fractures, surface flaw, and void, respectively

cohesion rather than embrittlement. The various fracture types observed in the warp fibres indicate that the warp likely experiences different structural stresses within the fabric. This may result from its function in upholding fabric tension and resilience. This hypothesis aligns with findings from similar studies, where warp fibres, being more highly oriented, exhibit diverse breakage modes due to their structural positioning and response to non-axial stress within the fabric matrix [49]. However, further investigation is required to determine whether this diversity of fracture types in the warp is uniquely linked to distinct degradation factors or merely reflects the warp's structural role in the fabric rather than indicating independent degradation mechanisms distinct from those affecting the weft.

4.3.3 Metal threads

Two types of metal threads were used in the textiles and analysed using VP-SEM-EDS: solid metal strips (Vt16) and solid metal strips wound around a silk core (Vt7, Vt17, Vt24 and Vt25). The solid metal strips included a double-sided silver-gilt strip (Vt16), while the metal strips wound around a silk core consisted of a silver-copper alloy (Vt7) and double-sided pure silver-gilt strips (Vt17, Vt24 and Vt25). A summary of the characterisation of these metal threads is provided in Table 3.

The strips wound around a silk core exhibit an S-twist direction of the metal coils (Vt17 and Vt24), except for the Vt25 sample, which shows both S- and Z-twist directions. The strips have thin diameters ranging from 188 to 375 μm and typically consist of two to three coils per unit length, following the Hacker et al. classification [52].

The EDS analysis of sample Vt16, a silver gilt strip (Fig. 9), confirmed that gilding was applied to both sides—a characteristic typical of metal strips produced using the 'cast, drawn, and rolled' technique [53–55]. This technique emerged in the early sixteenth century alongside advancements in wire manufacturing and involved flattening gilt silver wires and passing them through rollers. This process produced strips with a gold coating on both sides, which could be used as flat strips or wound around a core. Additionally, longitudinal striation lines were observed on the strip surfaces (Fig. 9a). These striations result from the drawing process, where metal strips are pulled through a drawplate before being flattened. Similar results have been documented in the literature [53, 54]. Regarding the gilding method employed, and considering that neither copper nor mercury was detected at the interface in the EDS analysis (data not shown), it is likely that traditional soldering involving copper or mercury-based fire gilding was not used [52]. Instead, an alternative heat-welding technique that did not rely on these elements may have been employed.

4.3.4 Inked cartouche

A very small loose fragment falling from a degraded area in the inked cartouche (Vt33) was collected to provide insights into the ink composition. Unexpectedly, the black colour was not derived from iron gall ink. Instead, FT-IR and SEM-EDS analysis suggested that the colour potentially originated from a carbon-based black pigment, most likely bone black. The presence of calcium phosphate

Table 3 Characterisation of metal threads collected from the garments

Sample ID/Item	High-resolution digital microscopic image	Description	Strip colour	Silk core colour	Thickness (μm)	wt.%	
						Ag	Cu
Vt7/Tunic (floral motifs)	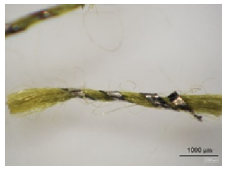	Silver-copper strip wound around a silk core	Silver	Green	29	97	3
Vt16/Tunic (sleeve)	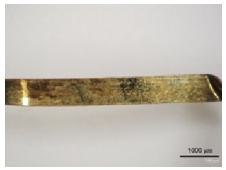	Double-sided silver-gilt strip	Golden	–	54	100	–
Vt17/Tunic (sleeve)		Double-sided silver-gilt strip wound around a silk core		Yellow	16	100	–
Vt24/Glove (metal lace)				White	7	100	–
Vt25/Sock (metal lace)		Double-sided silver-gilt strip wound around a silk core (crimped thread)		Yellow	9	100	–

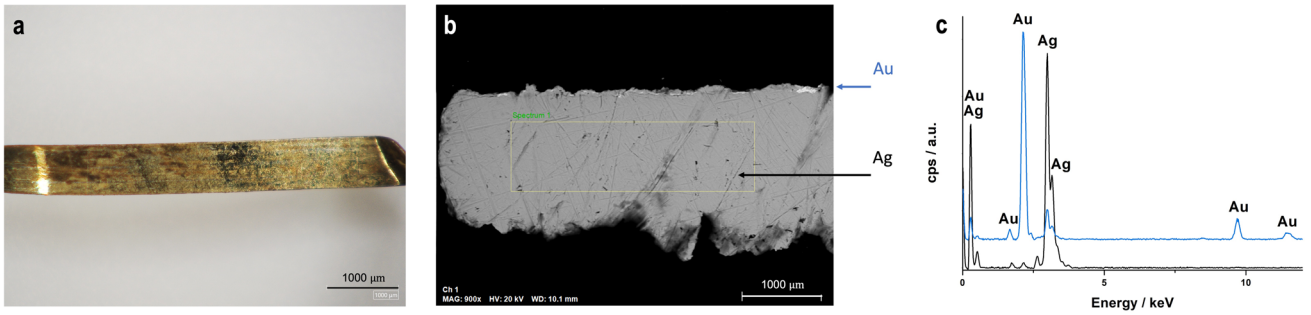

Fig. 9 **a** High-resolution digital microscopic image of the sample Vt16 (double-sided silver-gilt strip) from the tunic, **b** BSE image of the metal strip section, and **c** respective EDS area and point analyses

Table 4 Wavenumber (cm^{-1}), tentative assignment, and interpretation of the ATR-FT-IR analysis of the inked cartouche (sample Vt33)

Wavenumber (cm^{-1})	Assignment	Interpretation [57–59]
1619	$\nu C=O$	Amide I (silk) Calcium sulphate
1506	δNH and νCN	Amide II (silk)
1437	$\nu_3(CO_3^{2-})$	Calcium carbonate
1231	δNH and νCN	Amide III (silk)
1148	$\nu S=O$	Calcium sulphate
1020	νSO $\nu_3(PO_3^{4-})$	Calcium sulphate Calcium phosphate
1055	$\nu_3(PO_3^{4-})$	Calcium phosphate
869	$\nu_2(CO_3^{2-})$	Calcium carbonate
706	$\nu_2(CO_3^{2-})$	Calcium carbonate
669	$\delta\ (SO_4^{2-})$	Calcium sulphate
604	$\nu_4(PO_3^{4-})$	Calcium phosphate
560	$\nu_4(PO_3^{4-})$	Calcium phosphate

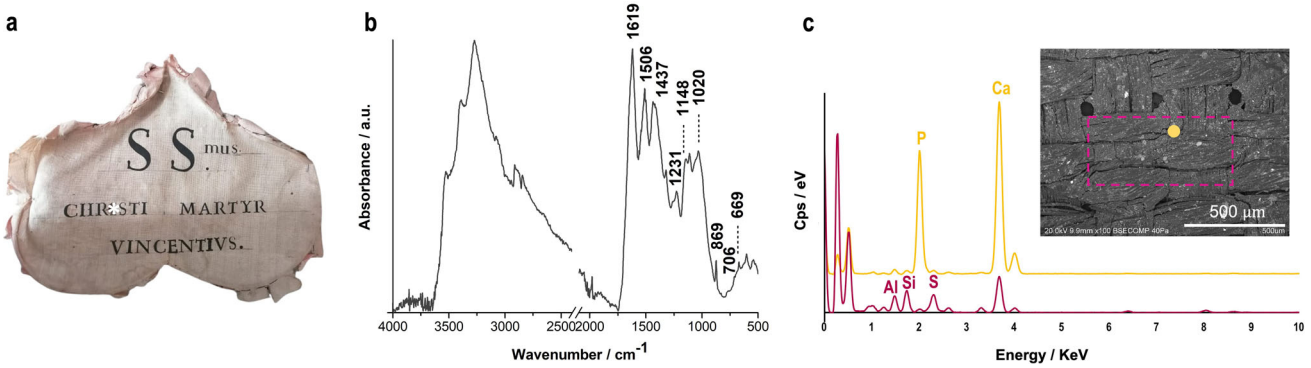

Fig. 10 **a** Photographic image of the inked cartouche with the area of the loose fragment (Vt33) marked with a white asterisk, **b** ATR-FT-IR spectrum of the inked area in sample Vt33, and **c** EDS spectra of the same area in (**b**) with corresponding BSE image

was confirmed by its characteristic IR features (Table 4), and P and Ca were detected through EDS analysis (Fig. 10c). Additionally, amide IR features (Table 4) were observed, confirming that the cartouche was composed of silk fabric. These features might also be contributed by protein-based binders that could potentially be used while preparing the bone black pigment [56]. Moreover, calcium carbonate and suphate were also observed in the FT-IR spectrum (Fig. 10 and Table 4), suggesting that the silk surface was pre-coated to improve pigment adherence.

4.3.5 Flower crown (paper)

A polychrome paper sample from the flower crown (Vt3) was analysed, and plant fibres were identified using OM (Fig. 11a). The ATR-FT-IR spectrum showed bands at *ca.* 3689 cm^{-1} (OH stretching), 524 cm^{-1} (Si–O–Al stretching), and 470 cm^{-1} (Si–O–Si

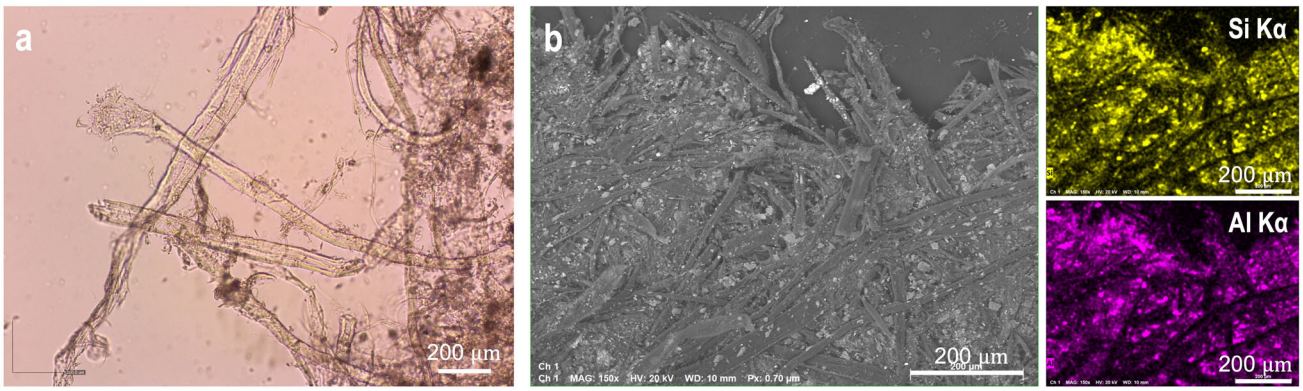

Fig. 11 **a** Optical microscopic image of sample Vt3 showing plant fibres, and **b** BSE micrograph of the paper sample with corresponding Si and Al elemental mapping

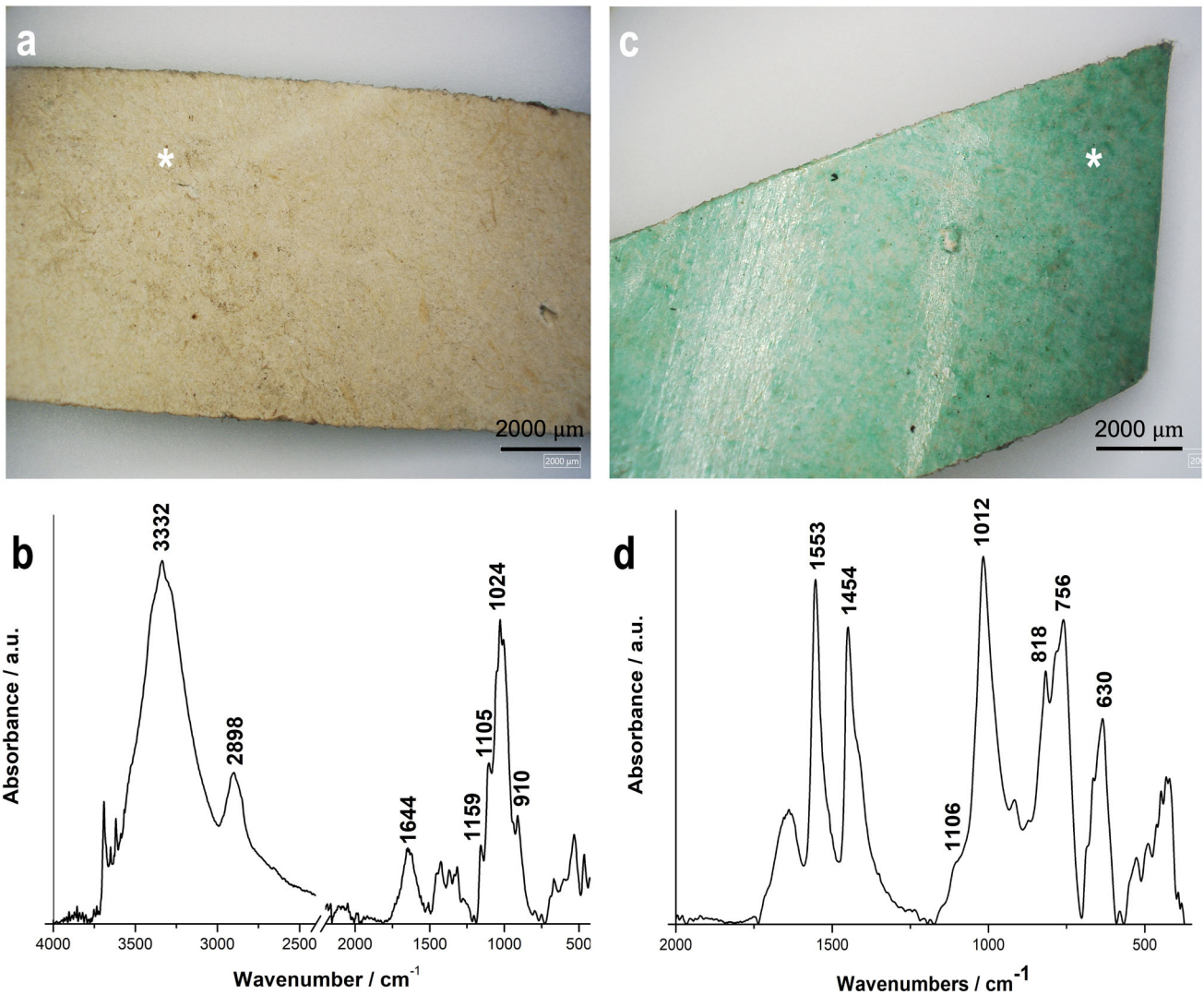

Fig. 12 High-resolution digital microscopic images of the paper sample Vt3 from the flower crown, **a** unpainted back side and **c** coloured front side; and respective FT-IR spectra, showing the characteristic features of **b** cellulose and **d** an emerald green pigment

bending), suggesting the presence of kaolin [60] (Fig. 12b). Additionally, EDS analysis confirmed the presence of aluminium silicate (Fig. 11b).

According to Bundy & Ishley [61], the use of kaolin as a filler dates back to the early nineteenth century, whereas its application as a coating became more common around 1870. Hubbe & Gill [62] further report that kaolin became the dominant filler in the paper industry in the early twentieth century. This mineral could have been applied in two ways: (1) as a filler material, added to the pulp during the paper manufacturing process, or (2) as a surface coating. Kaolin improves the physical and aesthetic properties of paper while reducing production costs [61, 62].

The identification of kaolin, along with OM observations indicating the absence of plant fibres like cotton or bast fibres, common in historical papermaking, suggests that softwood pulp was used as the primary source for the paper sample (Fig. 11a). Cotton and linen rags were the most common materials in early paper production, but their scarcity eventually led to the adoption of wood as a primary raw material [63]. By the nineteenth century, wood had become the preferred cellulose source for papermaking due to its abundance and low cost [60].

EDS analysis of the Vt3 coloured area indicated the presence of Cu and As, suggesting that a copper arsenite pigment was used. ATR-FT-IR complemented this analysis to discriminate the pigment. Figure 12d illustrates the resulting spectrum where typical features of emerald green pigment ($3Cu(AsO_2)_2{\cdot}Cu(CH_3COO)_2$) were observed. Bands at *ca.* 1553 and 1454 cm^{-1} are associated with ν_{as} and $\nu_s COO^-$, respectively, and 1012 cm^{-1} refers to δCH, ascribed to the pigment [64, 65]. Moreover, a small band at 818 cm^{-1} was attributed to the ν_sAsO vibration. A band at 630 cm^{-1} (δSO_4^{2-}) and a smooth shoulder at 1106 cm^{-1}, likely linked to νS=O, suggests that the sulphate process was used in the pigment's preparation [64–66]. The emerald green pigment was only introduced in 1800 and used until the end of the nineteenth century, placing this material within a timeframe consistent with the use of softwood pulp in papermaking and suggesting a production period within the nineteenth century, after the French invasions that affected the Major Seminary. Emerald green pigment is susceptible to degradation due to the migration of Cu or As ions from unreacted compounds, contributing to surface degradation over time [64, 65]. Notably, Fig. 12c shows brownish areas widely distributed over the paper surface, likely indicative of covellite (CuS), a common degradation product of copper-containing pigments [67].

5 Conclusion

The analytical investigation of Saint Vincent Martyr's simulacrum has provided invaluable insights into its material composition, craftsmanship, and the complex challenges associated with its preservation. This study revealed the simulacrum's layered construction while exposing severe osteological, textile, and chemical degradation caused by prolonged environmental exposure and historical events through a comprehensive array of imaging, microscopic, and spectroscopic techniques.

Key findings include the presence of softwood pulp paper containing kaolin fillers or coating, as well as emerald green pigment in the flower crown, pointing to 19th-century local reconstruction efforts likely aimed at restoring dignity to the relics after the devastation caused by the French invasions in 1810. These results reveal a dynamic interplay between Roman-origin elements and Portuguese adaptations, shedding light on the resourcefulness of local artisans in safeguarding the artefact's integrity. The analysis of wax and polychromed surfaces revealed intentional material applications, including incorporating calcium carbonate to enhance wax properties and using lead pigments and iron oxides to replicate human features.

The research further emphasises the importance of conservation strategies that balance respect for the artefact's materiality and historical authenticity with the integration of targeted preservation methods to ensure its longevity. Despite its fragility, Saint Vincent's simulacrum stands as a remarkable testament to religious artistry and devotion. This investigation not only protects its legacy but also establishes a framework for the study and preservation of similar artefacts, advancing heritage science and fostering a deeper appreciation for the intricate narratives embodied in religious simulacra.

Supplementary Information The online version contains supplementary material available at https://doi.org/10.1140/epjp/s13360-025-06405-x.

Acknowledgements The authors sincerely thank Father Nuno dos Santos, Dean of the Major Seminary of Coimbra, Father Calisto from the Seminary Archive and Eng. Paulo Morgado for the access to the simulacrum and support in the in situ campaign. We also acknowledge FCT for funding through the "Holy Bodies" Project (https://doi.org/10.54499/2022.01486.PTDC), J. Palmeirão and M. Nunes research fellowship and studentship, respectively. A. Manhita and A. Curto acknowledge FCT for financial support (https://doi.org/10.54499/CEECIND/00791/2017/CP1431/CT0005 and https://doi.org/10.54499/2020.02110.CEECIND/CP1593/CT0005, respectively). Funding was also provided through the strategic projects https://doi.org/10.54499/UIDP/04449/2020, https://doi.org/10.54499/UIDB/04449/2020 and IN2Past https://doi.org/10.54499/LA/P/0132/2020 (HERCULES Laboratory), UIDB/0622/2020 and UIDP/0622/2020 (CITAR).

Author contributions Conceptualisation: Joana Palmeirão and Teresa Ferreira; methodology: Joana Palmeirão, Teresa Ferreira and Margarida Nunes; validation: Margarida Nunes, Teresa Ferreira, Joana Palmeirão and Ana Curto; investigation: Joana Palmeirão, Margarida Nunes, Ana Curto, Teresa Ferreira and Ana Manhita; writing—original draft preparation: Joana Palmeirão, Margarida Nunes, Teresa Ferreira and Ana Curto; writing—review and editing: all authors; visualisation: Joana Palmeirão and Margarida Nunes. All authors have read and agreed to the published version of the manuscript.

Funding Open access funding provided by FCT|FCCN (b-on). Fundação para a Ciência e a Tecnologia, https://doi.org/10.54499/2022.01486.PTDC, https://doi.org/10.54499/2022.01486.PTDC, Joana Palmeirão, https://doi.org/10.54499/2022.01486.PTDC, Margarida Nunes, https://doi.org/10.54499/CEECIND/00791/2017/CP1431/CT0005, Ana Manhita, https://doi.org/10.54499/2020.02110.CEECIND/CP1593/CT0005, Ana Curto, https://doi.org/10.54499/UIDP/04449/2020, https://doi.org/10.54499/UIDB/04449/2020, https://doi.org/10.54499/LA/P/0132/2020, UIDB/0622/2020, UIDP/0622/2020.

Data availability The authors declare that the data supporting the findings of this study are available within the paper. Should any raw data files be needed in another format, they are available from the corresponding author upon request.

Declarations

Conflict of interest The authors declare that they have no conflict of interest.

References

1. P. Boutry, Moyen-Age Temps. Mod. (1979). https://doi.org/10.3406/mefr.1979.2519
2. S. Ditchfield, in *The Oxford illustrated history of the reformation*. ed. by P. Marshall (Oxford University Press, Oxford, 2015), p.152
3. D. Julia, in *Reliques modernes. Cultes et usages chrétiens des corps saints des Réformes aux révolutions*, ed. By P. Boutry, P.-A. Fabre, D. Julia, vol. I (Éditions de l'École de hautes études en sciences sociales, Paris, 2009), p. 69
4. J. Waterwort, *The canons and decrees of the sacred and œcumenical Council of Trent* (Dolman, London, 1848), pp.233–236
5. P. Boutry, in *Reliques romaines: invention et circulation des corps saints des catacombes à l'époque modern*. ed. by S. Baciocchi, C. Duhamelle (École française de Rome, Rome, 2016), p.225
6. S. Ditchfield, in *Martyrs and martyrologies*. ed. by D. Wood (Blackwells Publishers, Oxford, 1993), p.283
7. R.A. Lanciani, *Pagan and Christian Rome* (Houghton Mifflin Company, Boston and New York, 1892), pp. 328–360
8. S. Ditchfield, Stud. Church Hist. (2017). https://doi.org/10.1017/stc.2016.11
9. J.L. Bouza Álvarez, *Religiosidad contrarreformista y cultura simbólica del barroco* (Consejo Superior de Investigaciones Científicas, Madrid, 1990), pp. 81–157
10. P. Koudounaris, *Heavenly bodies. Cult treasures & spectacular saints from the catacombs* (Thames & Hudson, London, 2013), pp. 103–138
11. T. Johnson, J. Ecclesiast Hist. (1996). https://doi.org/10.1017/S0022046900012872
12. P. Boutry, P.-A. Fabre, D. Julia, *Reliques modernes. Cultes et usages chrétiens des corps saints des Réformes aux révolutions*, vol. I (Éditions de l'École de hautes études en sciences sociales, Paris, 2009)
13. P. Boutry, P.-A. Fabre, D. Julia, *Reliques modernes. Cultes et usages chrétiens des corps saints des Réformes aux révolutions*, vol. II (Éditions de l'École de hautes études en sciences sociales, Paris, 2009)
14. A. Burkardt, in *Les Cérémonies Extraordinaires du Catholicisme Baroque*. ed. by B. Dompnier (Presses Universitaires Blaise-Pascal, France, 2009), p.79
15. S. Baciocchi, P. Boutry, C Duhamelle, P.-A. Fabre, D. Julia, in *Pratiques du transnational. Terrains, preuves, limites*, edited by J.-P. Zúñiga (Centre de recherches historiques, Paris, 2011), p. 101
16. S. Baciocchi, C. Duhamelle, *Reliques romaines: invention et circulation des corps saints des catacombes à l'époque modern* (École Française de Rome, Rome, 2016)
17. J.-M. Ticchi, in *Reliques romaines: invention et circulation des corps saints des catacombes à l'époque moderne*. ed. by S. Baciocchi, C. Duhamelle (École Française de Rome, Rome, 2016), p.175
18. M. Ghilardi, *Il santo con due piedi sinistri. Appunti sulla genesi dei corpisanti in ceroplástica* (LuoghInteriori, Italia, 2019)
19. G. Sánchez Reyes, *Relics and Reliquaries in Colonial Mexico*. (Oxford University Press, Oxford, 2021), https://oxfordre.com/religion/view/10.1093/acrefore/9780199340378.001.0001/acrefore-9780199340378-e-964378.001.0001/acrefore-9780199340378-e-964 Accessed 21 June 2022
20. L.A. Kristóf, M. Kovács, G. Baksa, Z. Bereczki, F. Szatmári, L. Patonay, G. Pálfi, L. Pohárnok, J. Cult. Herit. (2015). https://doi.org/10.1016/j.culher.2014.04.001
21. A. Alterauge, T. Becker, B. Berndt, C. Jackowski, S. Lösch, RadioGraphics (2016) https://doi.org/10.1148/rg.2016150008
22. G.S. Reyes, J.L.V. Ramírez, A.L.M. Marrero, Ge-conservacion **10**, 54–65 (2016). https://doi.org/10.37558/gec.v10i0.370
23. A.C. Pfeiffer, Ph.D. thesis, Fachhochschule Köln (2005)
24. N. Prader, Master Thesis, Swiss Conservation-Restoration Campus (2012)
25. J.C. Palmeirão, Master Thesis, Universidade Católica Portuguesa do Porto (2015)
26. J.C. Palmeirão, Ph.D. Thesis, Universidade Católica Portuguesa do Porto (2023)
27. G. Mota, Boletim AUC. (2023) https://doi.org/10.14195/2182-7974_36_1_4
28. Major Seminary of Coimbra, Mapa das destruições que os Franceses fizeram no Seminario e nas suas Quintas, cx. 31, doc. 22, fol. 1 (unpublished)
29. J. Wiener, V. Kovačič, P. Dejlová, AUTEX Res. J. (2003). https://doi.org/10.1515/aut-2003-030202
30. J. Schlosser, *Historie du portrait en cire* (Macula, Paris, 1997)
31. M. Vandenbeusch, R. Stacey, D. Antoine, J. Archaeol. Sci. Rep. (2021). https://doi.org/10.1016/j.jasrep.2021.103186
32. J. Langlois, G. Mary, H. Bluzat, A. Cascio, N. Balcar, Y. Vandenberghe, M. Cotte, Stud. Conserv. (2017). https://doi.org/10.1080/00393630.2015.1131029
33. A. Montes Marrero, in XV Foro Académico - Bifurcaciones y Desiquilibrios Las Parad. La Restauración y El Património Cult. (Escuela de Conservacións y Restauración de Occidente, Guadalajara, 2018)
34. Y.C. Tang, Thesis, Universidad Complutense de Madrid (2021)
35. M. Regert, S. Colinart, L. Degrand, O. Decavallas, Archaeometry (2001). https://doi.org/10.1111/1475-4754.00036
36. M. Baglioni, G. Poggi, G. Ciolli, E. Fratini, R. Giorgi, P. Baglioni, Materials **11**, 7 (2018)
37. R. Chasan, D. Rosenberg, F. Klimscha, R. Beeri, D. Golan, A. Dayan, E. Galili, C.R. Spiteri, Soc. Open Sci. (2021). https://doi.org/10.1098/rsos.210950
38. M. Regert, J. Langlois, E. Laval, A.S. Le Hô, S. Pagès-Camagna, Anal. Chim. ActaChim. Acta (2006). https://doi.org/10.1016/j.aca.2006.06.038
39. L. Angelova, in *Ceroplastics: the art of wax*. ed. by R. Ballestriero, O. Burke, F.M. Galassi (L'Erma Di Bretschneider, Rome, 2019), p.169
40. D. Gramtorp, K. Botfeldt, J. Glastrup, K.P. Simonsen, Stud. Conserv. (2015). https://doi.org/10.1179/2047058413Y.0000000111
41. J.D. Rodriguez-Blanco, S. Shaw, L.G. Benning, Nanoscale (2011). https://doi.org/10.1039/c0nr00589d

42. V.J. Murrell, Stud. Conserv. (1971). https://doi.org/10.1179/sic.1971.012
43. R. Ballestriero, J. Anat. (2010). https://doi.org/10.1111/j.1469-7580.2009.01169.x
44. N. Eastaugh, V. Walsh, T. Chaplin, R. Siddall, *Pigment compendium: optical microscopy of historical pigments* (Routledge, Burlington, 2008)
45. E. Possenti, C. Colombo, M. Realini, C.L. Song, S.G. Kazarian, Anal. Bioanal. Chem. (2021). https://doi.org/10.1007/s00216-020-03016-6
46. F.C. Izzo, M. Kratter, A. Nevin, E. Zendri, ChemistryOpen (2021). https://doi.org/10.1002/open.202100166
47. E.S.B. Ferreira, A.N. Hulme, H. McNab, A. Quye, Chem. Soc. Rev. (2004). https://doi.org/10.1039/B305697J
48. J.W. Hearle, B. Lomas, W.D. Cooke. *Atlas of fibre facture and damage to textiles*, 2nd edn. (CRC Press, Manchester, 1998)
49. R.R. Bresee, G.E. Goodyear, Fractography of historic silk fibers, in *Historic textile and paper materials: conservation and characterization*. ed. by H.L. Needles, S. Haig Zeronian (American Chemical Society, Washington, DC, 1986), pp.95–109
50. J. Miller, B. Reagan, J. Am. Inst. Conserv. **28**, 97 (1989)
51. D. Nicodemo, J.E. Oliveira, A.A. Sedano, J.M. Marconcini, G.H.D. Tonoli, J. Mater. Sci. (2014). https://doi.org/10.1007/s10853-014-8355-4
52. A.-M. Hacke, Ph.D. Thesis, Manchester (2016)
53. A. Karatzani, X-Ray Spectrom. (2008). https://doi.org/10.1002/xrs.1021
54. A.-M Hacke, C.M. Carr, A. Brown, in Proceedings of Metal 2004, ed. By. J. Ashton, D. Hallam (National Museum of Australia, 2004), p. 415
55. M. Járó, Gold Bull. (1990). https://doi.org/10.1007/BF03214711
56. F. Ren, N. Atlasevich, B. Baade, J. Loike, J. Arslanoglu, Anal. Bioanal. Chem. (2016). https://doi.org/10.1007/s00216-015-9089-0
57. J.L. Perez-Rodriguez, A. Albardonedo, M.D. Robador, A. Duran, Microsc. Microanal. (2018). https://doi.org/10.1017/S1431927618015167
58. T. Mahendran, P.A. Williams, G.O. Phillips, S. Al-Assaf, T.C. Baldwin. J. Agric. Food Chem. (2008). https://doi.org/10.1021/jf800849a
59. M.A. Kasem, I. Yousef, Z.A. Alrowaili, M. Zedan, A. El-Hussein, J. Radiat. Res. Appl. Sci. (2020). https://doi.org/10.1080/16878507.2020.1752480
60. L.M. Proniewicz, C. Paluszkiewicz, A. Wesełucha-Birczyńska, A. Barański, D. Dutka, J. Mol. Struct. (2002). https://doi.org/10.1016/S0022-2860(02)00275-2
61. W.M. Bundy, J.N. Ishley, Appl. Clay Sci. (1991). https://doi.org/10.1016/0169-1317(91)90015-2
62. M.A. Hubbe, R.A. Gill. BioResources (2016). https://doi.org/10.15376/biores.11.1.2886-2963
63. F. Figueira, M. Matos, A. Nunes, M. Afonso, A.C. Rocha, J. Campelo, T. Ferreira. Conserv. Patrim. (2020). https://doi.org/10.14568/cp2019022
64. L.P. Munoz. Herit. Sci. (2024). https://doi.org/10.1186/s40494-024-01192-7
65. M. Vermeulen, S.M. Webb, S. Russick, A.C. McGeachy, K. Muratore, M.S. Walton, J. Hazard. Mater. (2023). https://doi.org/10.1016/j.jhazmat.2023.131453
66. D. Buti, F. Rosi, B.G. Brunetti, C. Miliani, Anal. Bioanal. Chem. (2013). https://doi.org/10.1007/s00216-013-6707-6
67. K. Keune, J.J. Boon, R. Boitelle, Y. Shimadzu, Stud. Conserv. (2013). https://doi.org/10.1179/2047058412Y.0000000063